THE JOURNAL OF PHYSICAL CHEMISTRY C
A JOURNAL OF THE AMERICAN CHEMICAL SOCIETY

pubs.acs.org/JPCC

Article

Combustion Reaction Dynamics of Nano-Aluminum and PVDF Composites, Part I: Experimental Studies at the Microscopic Level

Erik Hagen, Daniel Olsen, Yuxin Zhou, Min Zhou, and Michael R. Zachariah*

Cite This: *J. Phys. Chem. C* 2026, 130, 9351−9360

Read Online

ACCESS | Metrics & More | Article Recommendations | Supporting Information

ABSTRACT: In this Part I of a two-part series, we report the experimental characterization at the microscopic level of the propagation of printed Al/PVDF composites using high-speed microscopy and pyrometry. The focus is on quantifying the microstructure of the flame and the heterogeneous thermophysical properties of the reaction zone of materials with different loadings of aluminum nanoparticles (Al NPs). For the analyses carried out, three different Al NP loadings were used: 30, 40, and 50 wt %. It was found that, contrary to common expectations, there was no noticeable increase in the burn rate or the macroscopic flame temperature as the NP loading increased. High-speed microscopic images showed that the flame corrugation and microscopic burn rate also remained constant across the three loadings. The images also allowed the condensed-phase reaction zone to be analyzed, revealing that the zone thickness increased while the temperature gradient and the highest temperature decreased as the Al NP loading increased. The *in-operando* measured thermal diffusivity in the prereaction zone was found to increase with the Al NP loading. The observations and data obtained provide a basis for the development and calibration of a two-scale computational model in the Part II of this series. The first scale provides explicit particle−polymer and particle−particle microstructure effects. The second is a coarse-grained model that seeks to look at properties similar to those measured by the high-speed imaging.

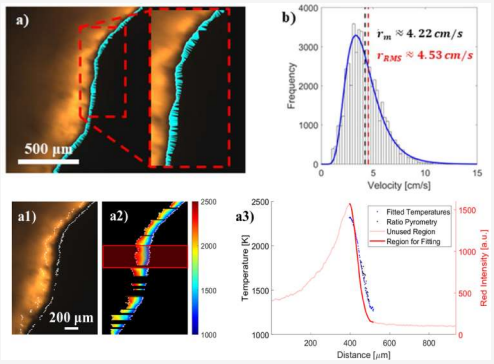

1. INTRODUCTION

Combustion of composite energetic materials, particularly those utilizing nanoscale metal powders as fuels with various oxidizers, is of interest for applications in propulsion and chemical warfare agent defeat.[1,2] However, a major difficulty in studying combustion systems is the inherent and complicated interplay of physics and chemistry during the reaction. This is particularly true in systems that have significant phase changes, such as those involving composite solids. Furthermore, modeling and validation are significantly hampered by the dearth of high-fidelity experiments in terms of providing the necessary information to ascertain potential mechanisms that must be captured, calibrated and validated.

Aluminum nanoparticles (Al NPs) are widely studied due to their high energy density and high specific surface area, which result in enhanced reactivity compared to bulk aluminum.[3−5] Their rapid oxidation and efficient heat release make them ideal candidates for applications in propulsion systems and energetic materials. The fine control over their size and morphology allows for tailored performance in reactive systems, further driving interest in them. The fluorination of aluminum fuel has been shown to be 2× more energetic than the oxidation of aluminum on a molar basis, and modern manufacturing techniques have allowed for the study of the interaction between fluoropolymers and fuel sources like aluminum nanoparticles and microparticles.[6−9] Polytetrafluoroethylene (PTFE or Teflon) is the highest F-containing fluoropolymer and has been studied with Al, but it is not readily soluble in most commercial solvents, making it difficult to study.[10,11] As a result, the next best candidate is polyvinylidene fluoride (PVDF) because it is the second highest F-containing fluoropolymer and is also readily soluble in many commercial solvents.[10]

This paper is **Part I** of a two-part study that integrates an experimental investigation and computational simulation. This integrated approach uses microscopic measurements of the thermal field in the first part to benchmark the multiphysics model development and computational analyses in the second part. We focus on a relatively simple composite system of aluminum nanoparticles in an oxidizer binder, PVDF, to facilitate tracking of key mechanisms in both experiments and modeling. The Al/PVDF composite, with different Al loadings, is in thin-film form created via ink printing. This system has previously been studied,[12,13] in part because the mechanical properties of PVDF lend themselves to being an excellent binder for metal powders at both the micro and nano scale, as

Received: January 28, 2026
Revised: May 10, 2026
Accepted: May 12, 2026
Published: June 23, 2026

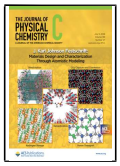

https://doi.org/10.1021/acs.jpcc.6c00579
J. Phys. Chem. C 2026, 130, 9351−9360

well as serving as the oxidizer for the fuel.[14−16] PVDF is known to release HF gas during decomposition, which serves as the oxidizer for the aluminum powder and exhibits interesting preignition chemistry between the alumina shell of the particles and the HF gas.[15,17]

The unique feature of this study is the use of high-speed microscopy and pyrometry to address gaps by providing high-resolution insights into the thermal field of the reaction. When these tools are applied to a conformal thin film, they enable us to track the flame front both spatially and temporally, allowing for a range of previously unmeasured properties and distributions to be studied. These properties include the extent of the corrugation and local burn vectors of the flame front. Due to the low corrugation of the flame front (<1.5), the thickness, temperature gradient, and peak temperatures can be measured from the thermal wave. The data is of sufficient fidelity to enable validation of a high-level phenomenological model, which will be presented in the second part of this two-paper series.[18]

2. EXPERIMENTAL SECTION

2.1. Materials

Aluminum nanoparticles (Al NPs, ∼100 nm, ∼92 wt % active, determined with TGA) were obtained from US Research Nanomaterials. Polyvinylidene fluoride (PVDF, average molecular weight: ∼534,000) was purchased from Sigma-Aldrich. N,N-Dimethylformamide (DMF, 99.8%) was purchased from Fisher Scientific.

2.2. Precursor Preparation and Direct Ink Writing of Free-Standing Films

The detailed procedures for direct ink writing to fabricate films can be found in our previous publication;[16] therefore, only a brief description is given here. To prepare the precursor solution, 375 mg of PVDF was dissolved in 5 mL of DMF. Al NPs were then added to the solution and sonicated for 30 min. After sonicating, the ink was stirred for 24 h. Just before printing, the solution was sonicated for another 30 min. The ink was then loaded into a 10 mL syringe with a 16-gauge needle (ID ∼ 0.7 mm) and extruded onto a heated glass substrate (∼75 °C) at a rate of ∼4.5 mL/h in a 3 cm × 3 cm square pad. Five layers were deposited on the glass substrate. After cooling, the pads were removed and cut into 1 cm × 0.3 cm sections for testing. The edges of the square (∼0.3 mm) were discarded to remove irregularities. Table 1 shows the formulation of precursors used in this work.

Table 1. Precursors for Samples

Sample Name	Al Powder [wt %]	Active Al [wt %]	Mass Powder [mg]	Mass PVDF [mg]	Volume DMF [mL]
A30	30%	27.6%	160.7	375	5
A40	40%	36.8%	250.0		
A50	50%	46.0%	375.0		

2.3. SEM/EDS

The morphologies and compositions of the cross-section of the printed films were characterized by scanning electron microscopy (SEM, Thermo Fisher Scientific NNS450) coupled with energy-dispersive X-ray spectroscopy (EDS).

2.4. High-Speed Imaging and Pyrometry

The high-speed imaging to understand flame structure and thermal field was conducted at two magnifications using a dual-camera setup. More information on the imaging setup can be found in our previous publications.[19−21] Briefly, microscopic images were captured using a high-speed color camera (Phantom VEO710L) coupled to a long working distance microscope lens (Infinity Photo-Optical Model K2 DistaMax, CF-4 Objective), which provides a spatial resolution of ∼1.7 μm/pixel from a working distance of ∼54 mm. Macroscopic images were taken with another high-speed color camera (Phantom Miro 110) with an aperture set at f/16. Details of the window size, frame rate, and exposure times for the different loadings can be found in Table S1 for the microscopic imaging and Table S2 for the macroscopic imaging.

Details of our three-color imaging pyrometry can be found in our previous studies.[21−23] Briefly, the raw intensities of the three-color channels (red, green, and blue) were extracted to construct color images. Ratios of the intensities of the three-color channels were used to estimate the temperature at that pixel, assuming graybody emission. Calibration factors were obtained by the response to a blackbody source (ThorLabs SLS201L and Micron M390). Temperatures obtained this way are filtered through a ratio uncertainty (∼0.15). More details can be found in the supplemental material. The expected error in the temperature is ∼200−300 K.

2.5. Flame Corrugation and Micro Burn Rate Measurement

In order to quantify the properties of the flame front at the microscopic level, it first needs to be located from the video frames. Color images were created from the demosaiced Bayer images in each frame. For each row of the image, the pixel intensity of the red channel was searched from right to left until a threshold was reached.

To assess how stretched a flame front is, we define a corrugation factor (right side of eq 7), which is the ratio of the stretched flame front (L_s) to the length of the unstretched flame front (L_u). L_s was determined by connecting the points drawn by the previously determined flame front. A flat flame front was determined for each frame by fitting the points of the current flame front to a straight line. The length of the flat flame front was determined by finding the length of the fitted line that would lie in the image window. Figure 1a−b show the diagram of this process, and Figure 4 shows the corrugated and flat flames.

We will consider the burn rates at two scales. The macro burn rate is the nominal burn rate measured by determining the regression rate. The micro burn rate is the local velocities measured by tracking the movement of the flame front at the pixel level, as shown in Figure 1b−c. Once the flame front profiles at two successive times are determined (the red line and blue line in Figure 1c), vectors (blue arrows) connecting the two flame fronts are constructed in such a manner that the vector lengths represent the shortest distances between the two fronts at their respective locations. The vector directions represent the local flame propagation, and the vector lengths are divided by the time period between the successive frames to yield the microscopic local flame front velocities. Thus, at each time, the "blue ladder" shown in Figure 1c comprises a set of micro velocities from which a histogram can be constructed later in Figure 5.

2.6. Flame Thickness and Temperature Gradient Measurement

To determine the properties of the condensed phase reaction zone, the zone must first be identified. It is important to note that in all videos, the flame propagated from left to right in the frame. To determine the reaction zone width in the horizontal direction, the light intensity of the red channel was extracted from the demosaiced color images. In each image, there may be multiple peaks due to ejections of post-products; as a result, the rightmost peak was chosen and assumed to be the end of the reaction zone. To determine the onset of the reaction zone, the spatial gradient of the light intensity (in the horizontal direction) is used to determine when the gradient approaches zero. This point is assumed to be the onset of the reaction. An example of the reaction zone can be seen in Figure 2a, where the temperatures determined with three-color pyrometry within the reaction zone are shown as black dots. It should be noted that not all temperatures within the reaction zone estimated with pyrometry are within the uncertainty tolerance. As a result, an effective emissivity (ϵ_{eff}) to relate light intensity and temperature was estimated for each run. To generate the ϵ_{eff}, pixels with both an intensity and a temperature inside each reaction zone were extracted.

https://doi.org/10.1021/acs.jpcc.6c00579
J. Phys. Chem. C 2026, 130, 9351−9360

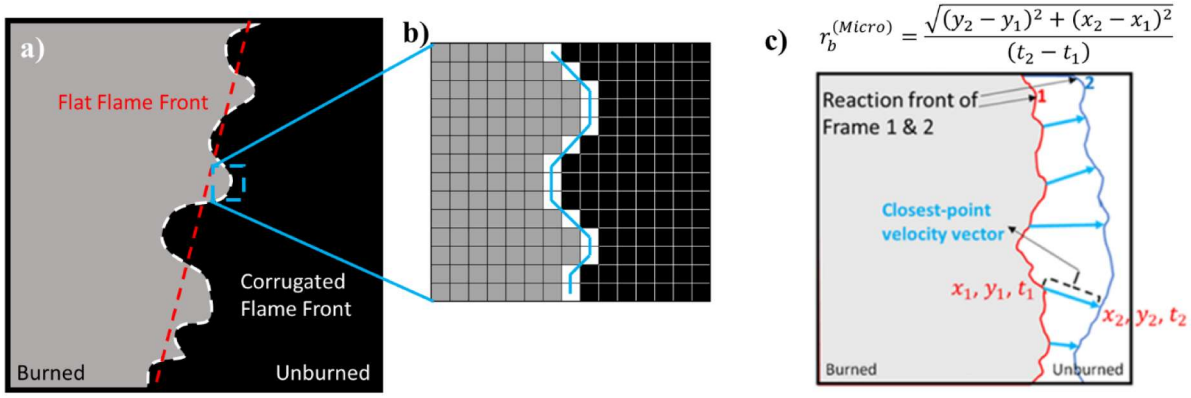

Figure 1. (a) Depiction of corrugated (white) and flat (red) flame fronts. (b) The white boxes represent the pixels associated with the flame front. The blue line, going from center to center of the pixels, is the length of the flame. (c) Calculation of the micro velocities.

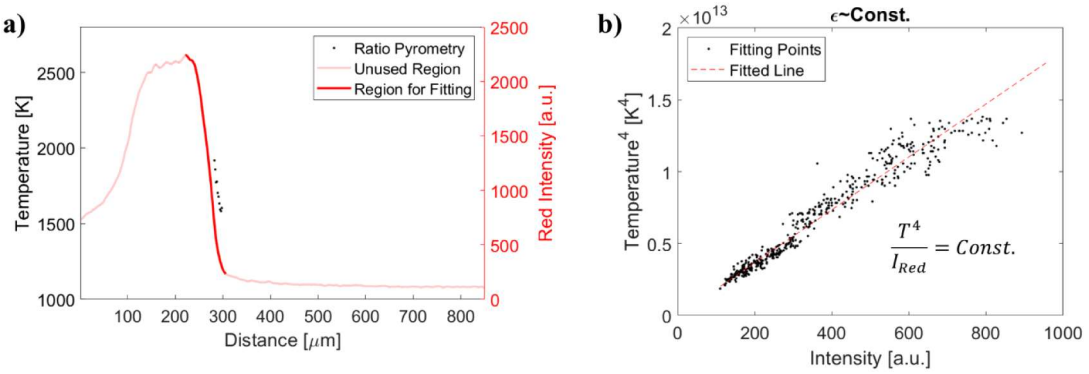

Figure 2. Measured temperature profile: (a) Intensity profile across the row of a single frame. The dark red line is the reaction zone. The black dots are the temperatures obtained from ratio pyrometry. (b) A fit of the emissivity constant. The black dots were obtained from ratio pyrometry.

Then, using the Stefan−Boltzmann law (eq 1), an ϵ_{eff} was determined as

$$\epsilon_{\text{eff}} = \frac{T^4}{I} \tag{1}$$

where, I is the intensity of the red channel and T is the temperature from three-color pyrometry. The determined ϵ_{eff} was applied to the intensity curve of the reaction zone to yield the temperature profile. This enables us to measure temperature directly from the calibrated light intensity. With this definition, the ϵ_{eff} would behave as the inverse of the real emissivity; however, given that this is simply a tool to extract temperature, ϵ_{eff} is not used to extract an absolute emissivity.

Once the reaction zones and the temperature profiles are measured, thermal wave thicknesses, temperature gradients, and peak temperatures of the reaction zone can be evaluated. The thermal wave thickness was determined by finding the length of the reaction zone on the image and then multiplying it by the distance-to-pixel ratio (~1.7 μm px^{-1}). The temperature gradient was determined by performing a linear regression to fit a first-order polynomial on the position and corresponding temperatures. The slope of this fit gives the temperature gradient. The effect of filtering temperature gradients by an R^2 value can be seen in Figure S16. There was no noticeable variance, and an R^2 of 0.9 was chosen here. The onset and maximum temperatures are assessed directly from the measured temperature profile.

2.7. Preheat Zone Thermal Diffusivity Measurement

Flame propagation requires thermal transport from the flame to the preheat zone. Thermal diffusivity was determined under the assumption that no reaction takes place in the preheat zone, as stated in our previous publication.[22] In short, the thermal diffusion equation (eq 2) can be rewritten by substituting $t = x/r_B$; where r_B is the burn rate, with the assumption of a steady-state propagation rate. If it is also assumed that in the prereaction zone, that there is an exponential relationship between temperature and position (eq 3), then, by taking the proper derivatives eq 2 can be rearranged as eq 4.

$$\frac{\partial T}{\partial t} = \alpha \frac{\partial^2 T}{\partial x^2} \tag{2}$$

Where T is temperature, t is time, α is the thermal diffusivity, and x is the position.

$$T(x) = A \times \exp(bx) \tag{3}$$

b is the exponential coefficient.

$$\alpha = \frac{r_B}{b} \tag{4}$$

Details on the effect of an R^2 value can be seen in Figure S17. In this study, an R2 value of 0.5 was used. Going to higher values removes more than 80% of the measured values, concentrating the remaining points on an isolated value. The chosen threshold balances the goodness of fit with the retention of sufficient data for reliable trends.

3. RESULTS AND DISCUSSION

3.1. Al-PVDF Film Combustion

Three Al/PVDF thin-film composites were made by direct ink writing, with 30, 40, and 50 wt % Al NPs. Films with a loading below 30 wt % Al NPs could not be imaged with the microscopic camera, as during combustion, the films expand and move outside of the focal plane of the camera. Films with a loading exceeding 50 wt % Al NPs could not be printed. We

https://doi.org/10.1021/acs.jpcc.6c00579
J. Phys. Chem. C 2026, 130, 9351−9360

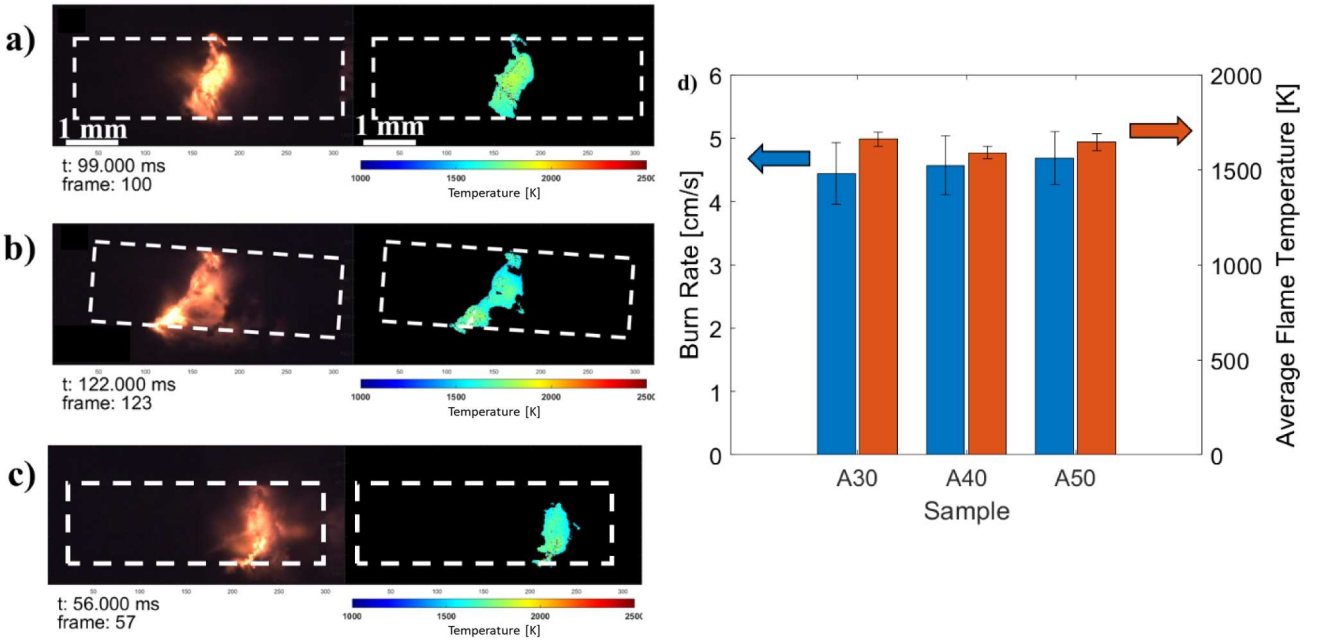

Figure 3. (a–c) Macro-scale images of the Al-PVDF film combustion for 30, 40, and 50 wt % Al NPs, respectively. The left-hand image is a color image, and the right-hand image is a false-color temperature map. d) Comparison of the average burn rate and flame temperature for the three films.

attribute the printability issue to the interparticle spacing. More discussion is available in the Supporting Information regarding the interparticle spacing (Section S6). Assuming the overall combustion follows eq 5 it was determined that the equivalence ratio of these films is fuel-rich ranging from ~1.4–3.3. SEM/EDS was used to investigate the cross-sectional film thickness and Al NP dispersion in the PVDF matrix. SEM (Figure S7-1) images show that the thickness of the films is ~60–100 μm. EDS mapping of Al and F indicates a consistent dispersion of Al nanoparticles throughout the PVDF matrix, with no significant agglomerations observed (Figure S7-2 and 3).

$$2\,\mathrm{nAl} + 3(\mathrm{C_2F_2H_2})_n \rightarrow 2\,\mathrm{nAlF_3} + 3\mathrm{nH_2} + 6\mathrm{nC} \quad (5)$$

The burn rate and flame temperature were analyzed with high-speed imaging (Phantom Miro M110) and three-color pyrometry. Snapshots of the combustion captured with this camera can be seen in Figure 3a–c. The films were ignited by a resistively heated NiCr wire and burned in an argon environment. The macroscopic burn rate was estimated by tracking the leading edge of the burn front across multiple frames. The pixel distance was converted to centimeters using the camera's spatial resolution, and then position vs time scatters were fit to a straight line. The slope of this line was assumed to be the burn rate.

In previous studies, it was shown that increasing the active Al content from ~15–50 wt % increased the burn rate from ~2–10 cm s^{-1}.[16] The burn rate was also unaffected by the thickness of the film. The films presented in this study, however, did not show an increase in velocity with Al loading. The average burn rate of the films went from ~4.5 to 4.7 cm s^{-1} as the loading of active Al increased from ~28–45 wt % active Al (Figure 3d). Part of this overall decrease in reactivity is attributed to the wide distributions of diameters in the Al powder used in this study compared to that used in previous studies.[24] SEM of the powder used in this study shows that there are many micron-scale particles in the powder (Figure S10). However, this trend is likely better explained by the porosity (P) of the composites. In this case, the porosity of the films increases from ~0.2–0.4 (Table S4), which is the opposite trend reported by other direct ink writing methods.[25] This would cause the effective thermal diffusivity to not scale as quickly as expected, retarding heat transfer and, in turn, the burn rate. Table 2 shows measured thermal diffusivities (α) and reaction zone thicknesses (δ), which can be used to estimate the expected trend of the burn rate.

$$r_b \sim \frac{\alpha}{\delta} \quad (6)$$

Table 2. Averages and Standard Deviations Measured Thermo-Physical Properties

	Thickness [μm]	Temperature Gradient [K μm^{-1}]	Max Temperature [K]	Thermal Diffusivity [10^{-5} m^2 s^{-1}]
A30	95.8 ± 21.2	15.8 ± 5.7	2354 ± 209	6.5 ± 1.3
A40	138.2 ± 25.5	8.7 ± 2.9	2219 ± 212	7.2 ± 2.0
A50	141.6 ± 3.6	3.9 ± 1.9	1927 ± 197	7.7 ± 1.2

Normalized values for measured burn rates and values calculated with eq 6 can be seen in Figure S15. The two trends for these normalized burn rates have a close relationship, suggesting that the burn rate flatness is associated with the physical properties of the system.

While the burn rate did not show the same trend, the flame temperature is consistent with prior work. Both show no change with loading and remain constant at ~1500–1700 K (Figure 3d). These temperatures agree well with previous publications' estimations of the adiabatic flame temperature.[26] A more detailed discussion and comparison is outlined in Section 3.3.

https://doi.org/10.1021/acs.jpcc.6c00579
J. Phys. Chem. C 2026, 130, 9351–9360

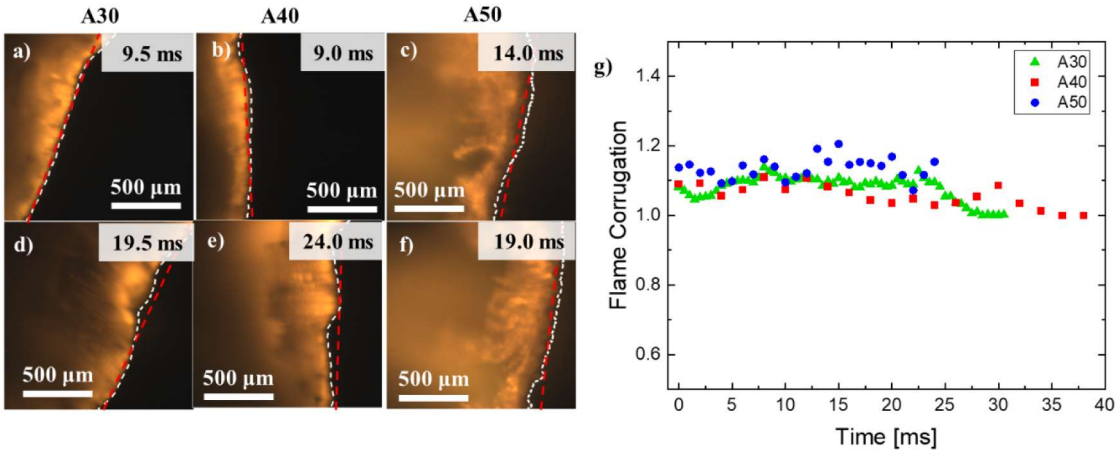

Figure 4. Snapshots showing the corrugated flame (L_s) (white) and the flat flame (L_u) (red). (a, d) are 30 wt %. (b, e) are 40 wt %. (c, f) are 50 wt %. g) Corrugation ratio with time.

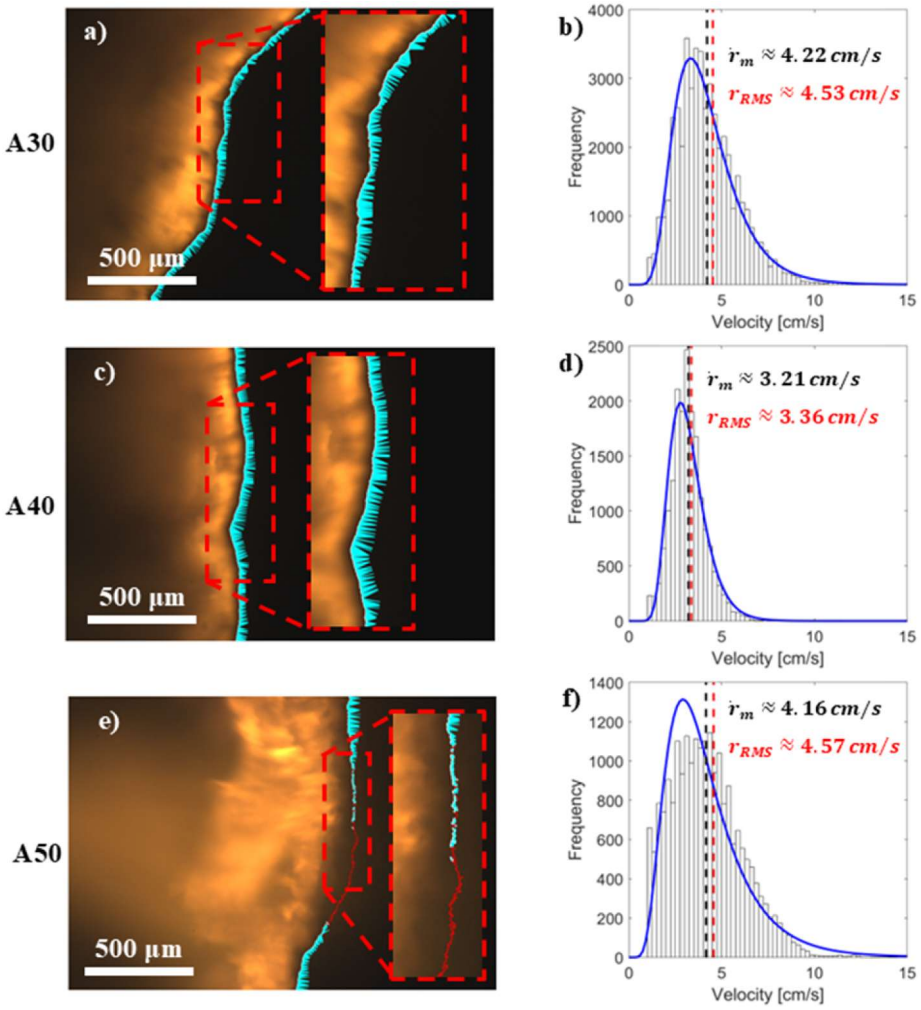

Figure 5. (a, c, e) Microscopic snapshots of the flame front of 30, 40, and 50 wt % Al NPs, respectively. The blue lines are burn vectors. The red line represents locations where a burn vector could not be determined. (b, d, f) Distributions of micro velocities for the corresponding particle loading. The blue line represents a log-normal fit. The black line corresponds to the average of the distribution, and the red line corresponds to the RMS of the distribution.

3.2. Microscopic Flame Structure Analysis

High-speed microscopy (Phantom VEO710L, K2 DistaMax) revealed three different modes of combustion for the three loadings of the Al NPs. At the lowest loading (A30), no dispersed or condensed-phase products are observed, as seen in Figure 4a,d. Instead, the products stay attached to the reaction zone and leave behind a stretched-out, fibrous, black product (Figure S9). The A40 and A50 samples both had

https://doi.org/10.1021/acs.jpcc.6c00579
J. Phys. Chem. C 2026, 130, 9351−9360

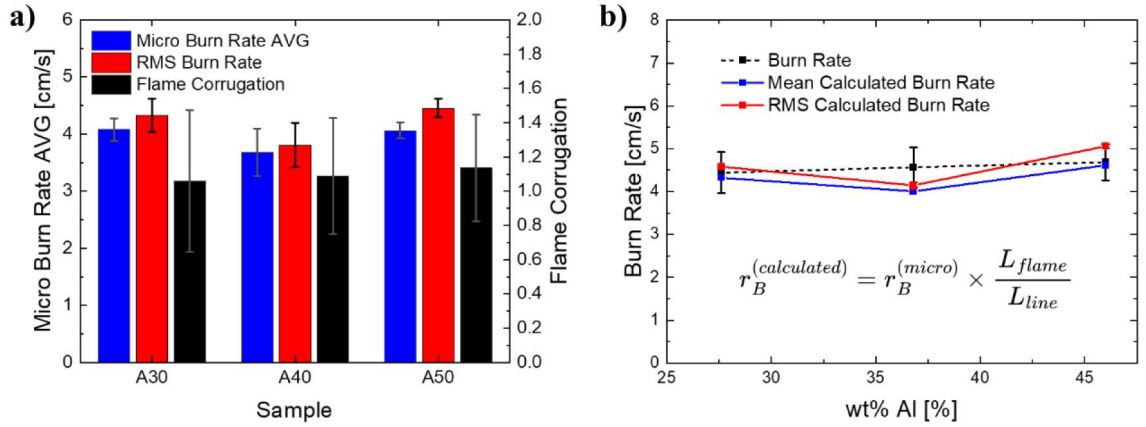

Figure 6. (a) Micro flame front properties. (b) Comparison of the measured and estimated burn rates.

ejections from the reaction zone. A40 shows that large flakes break off in large chunks from the burning surface, while the A50 sample shows smaller, more frequent ejections. Examples of the microscopic images can be seen in Figure 4b,e for A40 and Figure 4c,f for A50.

Studies assessing the stretching of the flame, the corrugation factor, and the micro burn rate ($r_b^{(\text{micro})}$) of the flame front have been done in the past, enabling a connection between the observed global burn rate and the microscopic properties eq 7.[20,27,28]

$$r_b^{(\text{global})} \approx r_b^{(\text{calculated})} = r_b^{(\text{micro})} \times \frac{L_s}{L_u} \tag{7}$$

where $r_b^{(\text{global})}$ is the measured burn rate from macroscopic imaging, and $r_b^{(\text{calculated})}$ is the calculated burn rate based on an assumption that the local burn rate times the flame length should yield a value close to the observed macro burn rate. Thus, here we define $r_b^{(\text{micro})}$ as the local microvelocity, and L_s/L_u is the corrugation factor, where L_s is the length of the stretched flame front, and L_u is the length of the unstretched flame front.

The basic premise behind eq 7 is that the microburn rate is more closely associated with the local chemistry and transport lengths, which are most closely associated with composition. This parameter can be thought of in a manner analogous to the laminar flame speed in premixed gas flames. The flame stretch, then, is a parameter that is more closely related to the architecture of the system. The product should thus give the observed macroscopic burn rate or, in keeping with the gas-phase analogue the turbulent flame speed.[20,27,28]

The length of the unstretched flame was calculated from a linear fit of the stretched flame front inside the window, which was used to measure the corrugation factor. Figure 4a–f shows example images of L_s and L_u. Using this new approach, the L_s/L_u was found to be constant with time for each of the three loadings. Taking the averages, L_s/L_u appeared to increase from ~1.05–1.15, resulting in a 1.07× increase. This increase is similar to that of $r_b^{(global)}$ which is 1.05×. First, this low corrugation factor is another good indicator of homogeneously dispersed Al NPs in the PVDF matrix, further confirming what was shown with the EDS maps. Heterogeneity in the dispersion of Al NPs would have caused pockets of particles that would have increased the corrugation factors by creating local hot spots.[27] Second, the small increase in $r_b^{(\text{global})}$ is likely attributed to this corrugation factor.

The microburn rates $r_b^{(\text{micro})}$ were measured by finding the closest points between subsequent flame fronts. Unphysical burn vectors (going backward, touching the edge of the frame, etc.) were not considered when generating distributions. Due to the high number of points, distributions of the magnitude of the velocities have been plotted and fitted to log-normal distributions for each of the loadings. Previous publications studying microflame velocities have seen similar trends.[27,28] In Figure 5, the left-hand column of images are snapshots of A30, A40, and A50 with the local velocity vectors of the flame fronts overlaid. The right-hand column of images shows the corresponding distribution for that run. Figure 6a shows the averages of multiple runs of the microscopic flame front properties measured.

Previous publications have reported averages (r_m) of these distributions as $r_b^{(\text{micro})}$ with varying degrees of success in relating the global and microscopic properties. When the average was used, the calculated burn rate was always underpredicted. It was found for this system that the root-mean-square velocity ($rRMS$) of the distribution as $r_b^{(micro))}$ shows a better estimation of $r_b^{(\text{global})}$. Figure 6b shows the calculated burn rate using both r_m and r_{RMS} velocities from the distributions. As the loading of the Al NPs increased, both r_m and r_{RMS} appear to stay consistent.

3.3. Thermo-Physical Properties

The burn rate is a relatively easy metric to measure experimentally for model calibration; however, more information can be extracted from the high-speed microscopy images. Due to the flame front being relatively flat, we can assume that this experiment is quasi-1D. As a result, a condensed phase reaction zone can be located for each row on an image and probed for useful properties in order to validate the results in Part II[18] of this study. From these, flame thicknesses (δ), temperature gradients (∇T), and peak temperatures ($T_{\max}$) of the reaction zone can be determined, as well as thermal diffusivities (α) of the prereaction zone. In order to do this, reaction zones were located, and an effective emissivity (ϵ_{eff}) was used with eq 1 to estimate temperatures along the reaction zone. With this definition, the ϵ_{eff} prescribed in eq 1 would go as the inverse of the real emissivity; however, given that this is simply a tool to extract temperature ϵ_{eff} is not used to extract

https://doi.org/10.1021/acs.jpcc.6c00579
J. Phys. Chem. C 2026, 130, 9351–9360

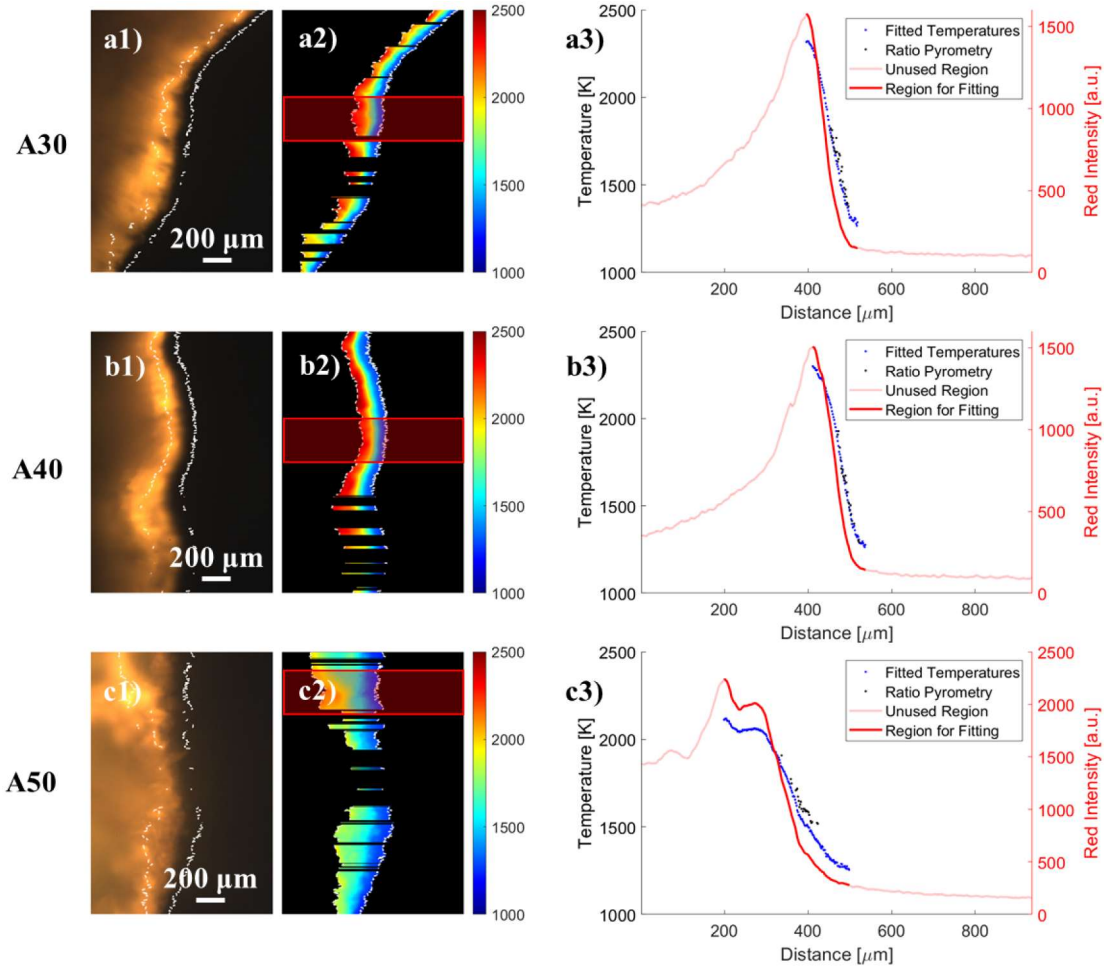

Figure 7. (a, b, c) A30, A40, and A50 samples, respectively. 1) Microscopic snapshots of the reaction zone. The white lines represent the bounds of the reaction zone. Propagation goes from left to right. 2) Temperature maps of the reaction zones using the emissivity fit. 3) Intensity profiles of a single row inside the red boxes in 2. The dark red line is the reaction zone. The blue dots show the fitted temperatures, and the black dots show the pyrometry temperatures.

an absolute emissivity. The real emissivity depends on many variables, including but not limited to temperature, surface roughness, wavelength, composition, etc., and cannot be evaluated using methods described here.[29−31] Distributions of ϵ_{eff} for single runs can be seen in Figure S4. Figure 7a−c,1 shows color images of the A30, A40, and A50 reaction front, and Figure 7 a−c,2 shows the corresponding temperature maps. Black portions of the temperature maps are points either outside of the reaction zone or where reaction zones could not be located. Figure 7a−c,3 shows single reaction zones with both the temperatures from three-color pyrometry and the temperatures from the fitted ϵ_{eff} are shown and appear to have good agreement with each other.

Similarly to the micro velocities, distributions of each of these properties can be generated, and sample distributions for A30 can be seen in Figure 8 and similar distributions can be seen in Figure S2 and Figure S3 for A40 and A50, respectively. Averages and average standard deviations of multiple distributions (multiple runs) can be seen in Table 2. When looking at the distributions, δ, ∇T and α all appeared to have a log-normal distribution, while $T_{\max}$ showed a more normal distribution. While it is not totally understood why this is the result, some conclusions can still be drawn; namely, the relationship between the RMS velocity and α. For a premixed gas flame, it is known that laminar flame velocity is proportional to the square root of the thermal diffusivity ($S_L^0 \propto \sqrt{\alpha}$).[32−34] If it is assumed that the system operates on the averages of these thermo-physical properties and follows a similar trend when relating the local velocity and the α, then it is reasonable to assume that the RMS velocity should better represent $r_b^{(\text{micro})}$.

Looking at the averages of these properties, it can be seen that α and δ both increase with increased powder loading, while $T_{\max}$ and ∇T decrease. Values of α for both the solid and liquid phases of Al have been reported previously.[35] The values of the measured α in this study show good agreement with the α of solid Al reported in[35] suggesting that the Al has not begun to melt in the prereaction zone. The increase in α in the composite is attributed to the increase in Al loading. This increase allows for better heat feedback to the unreacted zone, resulting in an increase in reaction zone thickness, δ. The temperatures reported for $T_{\max}$ are much higher than the temperatures reported in Figure 3c. This is due to the spatial resolution limitation of the macroscopic camera. While the microscopic camera allows for around 60−80 pixels for each reaction zone, the macroscopic camera has around 3−4 pixels. This means that one pixel for the macroscopic camera is seeing

https://doi.org/10.1021/acs.jpcc.6c00579
J. Phys. Chem. C 2026, 130, 9351−9360

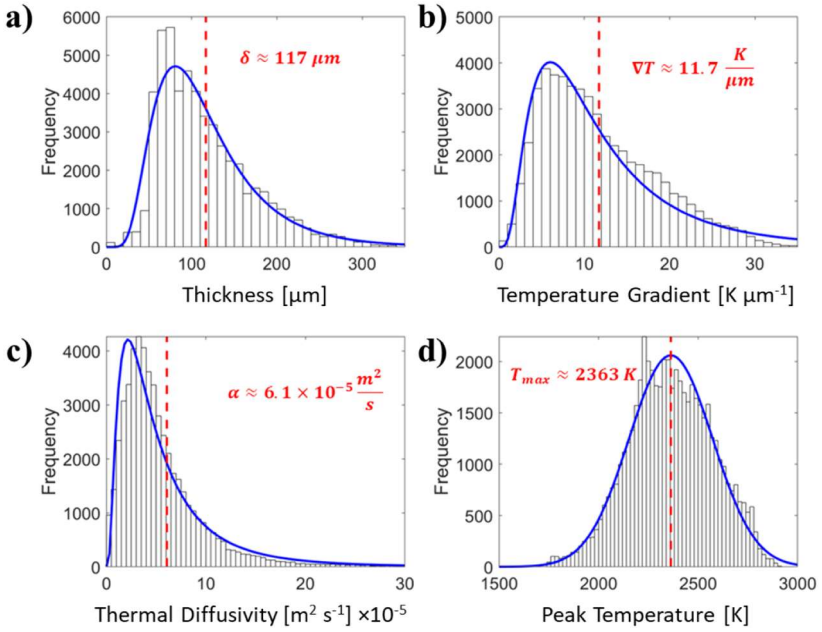

Figure 8. Distributions of each thermo-physical property for one video of an A30 sample. For each distribution, the blue line represents a log-normal or normal fit to the histogram. The red line shows the average of that distribution. (a) Flame thickness (log-normal). (b) Temperature gradient (log-normal). (c) Thermal diffusivity (log-normal). (d) Maximum temperature (normal).

a wider distribution of temperatures and, as a result, reporting approximately the average temperature of the reaction zone.

Thermochemical calculations have been done previously for an Al/PVDF system, the details of which are presented in another study.[26] Örnek et al. estimated the heat of formation ($\Delta_f H°$) of PVDF to be ∼−480 kJ/mol using a group-contribution method.[26,36−38] This estimation led to temperatures ranging from ∼1925−1625 K as the loading of active Al changed from ∼25−40 wt %, agreeing well with the macroscopic temperature measured. For this study, the $\Delta_f H°$ was estimated using group additivity.[36,39,40] Chains of $-CF_2-CH_2-$ were generated, and the heat of formation was estimated from 1 to 15 monomers. Due to the nature of the estimation, there were two extra H atoms for each input. This yielded a $\Delta_f H° \approx -426 kJmol^{-1}\,(\#ofMonomers)^{-1}$ (Figure S5), which is very similar to previously estimated values. Using this heat of formation, Cheetah was used to carry out chemical equilibrium calculations. This resulted in temperatures of ∼2250−1750 K across ∼25−45 wt % Al (Figure S6). Interestingly, these temperatures are much closer to T_{max}. Regardless of which $\Delta_f H°$ is correct, the decrease in T_{max} is attributed to the composite becoming more fuel-rich. It can also be seen from these calculations that the production of AlF gas increases, and the production of HF gas decreases with increasing Al (Figure S6). From the decrease in ∇T it can be seen that the change in reaction zone thickness plays a bigger role than the change in temperature across the reaction zone.

As stated previously, there is a temperature uncertainty of ±300 K, and as a result, an uncertainty quantification of temperature-sensitive properties is considered here. Since the thickness was not measured using temperature, it was excluded from this analysis. To do this, an offset temperature (ΔT) ranging from −300 K to +300 K was applied to the pyrometry measurements (T_{pyro}) to compute an uncertainty-biased emissivity.

$$\tilde{\epsilon}_{eff} = \frac{(T_{pyro} + \Delta T)^4}{I} \tag{8}$$

$\overline{\epsilon}_{eff}$, was applied to the red intensity field, as before, to enable an assessment of its effect on temperature uncertainty. The method used to estimate the thermal diffusivity of the prereaction zone is not sensitive to variations in the effective emissivity, as demonstrated in Section S10. This insensitivity is a result of the specific approach for determining α and does not imply that the thermal diffusivity is independent of temperature in a physical sense. Rather, it reflects a limitation in the current experimental setup, where the temperature dependence of α cannot be precisely quantified at this stage. Nevertheless, the temperature gradient and maximum temperatures remain important variables to analyze.

Figure S13 shows histograms for single runs, similar to Figure 8(b) and (d). Figure S14 shows curves of both the temperature gradient and max temperatures vs ΔT. Each property, at all loadings, increased monotonically with ΔT and is nearly linear. To assess the effect of the temperature uncertainty, two metrics were defined. The first, β_X (eq 9), is the difference in the average values at ΔT_{max}=300 K and ΔT_{min} = −300 K. An example of β can be seen in Figure S14.

$$\beta_X = X(\Delta T = +300K) - X(\Delta T = -300K) \tag{9}$$

Where X is either ∇T or T_{max}. The second, $\xi_X^{(30,40)}$ and $\xi_X^{(40,50)}$, represent the average differences between 30−40 wt % nAl and 40−50 wt % nAl, respectively, evaluated across ΔT.

$$\xi_X^{(30,40)} = \frac{1}{\Delta T_{max} - \Delta T_{min}} \int_{\Delta T_{min}}^{\Delta T_{max}} (X_{40}(\Delta T) - X_{30}(\Delta T))\, d(\Delta T) \tag{10}$$

https://doi.org/10.1021/acs.jpcc.6c00579
J. Phys. Chem. C 2026, 130, 9351−9360

$$\xi_X^{(40,50)} = \frac{1}{\Delta T_{max} - \Delta T_{min}} \int_{\Delta T_{min}}^{\Delta T_{max}} (X_{50}(\Delta T) - X_{40}(\Delta T)) \, d(\Delta T) \quad (11)$$

As such, if $\beta < \xi$ then this property is more sensitive to the nAl loading than the temperature uncertainty, and if the opposite is true, then the property is more sensitive to the temperature uncertainty. Values for β_X and both ξ_X's can be seen in Tables 3 and 4 respectively. For ∇T, both $\xi_{\nabla T}^{(30,40)}$ and $\xi_{\nabla T}^{(40,50)}$, are greater than ∇T near their respective loadings, while for T_{max}, βT_{max}, is greater than both $\xi_{Tmax}^{(30,40)}$ and $\xi_{Tmax}^{(40,50)}$. This means that the temperature gradient is more sensitive to the loading of the nAl in the composite, which is also the case for the thickness of the thermal wave. On the other hand, the max temperature appears to be heavily influenced by the temperature uncertainty β rather than the aluminum loading. Overall, these results establish that the temperature uncertainty impacts the max temperature, while the gradient in the temperature is predominantly controlled by the nAl loading. This distinction is critical for interpreting the experimental data and provides necessary trends and uncertainty for **Part II** of this work.

Table 3. Values of β_X

Sample	$\beta_{\nabla T}[K\ \mu m^{-1}]$	$\beta_{T_{max}}[K]$
A30	6	825
A40	3	810
A50	1	700

Table 4. Values for $\xi_X^{(30,40)}$ and $\xi_X^{(40,50)}$

$\xi_{\nabla T}^{(30,40)}[K\ \mu m^{-1}]$	$\xi_{\nabla T}^{(40,50)}[K\ \mu m^{-1}]$	$\xi_{Tmax}^{(30,40)}[K]$	$\xi_{Tmax}^{(40,50)}[K]$
9 ± 1	4 ± 0.5	110 ± 4	290 ± 30

4. CONCLUSION

The burning of Al NPs in a PVDF oxidizer/binder has been studied using high-speed imaging and high-speed microscopy to relate bulk properties to microscopic properties and to develop a data set that is useful for developing and validating models of the Al-PVDF reaction. It was found that the burn rate and flame temperature were not significantly affected by the loading of Al NPs, despite the fact that the system's overall stoichiometry was changed. High-speed microscopy found that the small change in burn rate can be attributed to the corrugation of the flame front and not the microscopic burn rates. Distributions of the microburn rates were shown to be mostly log-normal. It was also found that the thermal diffusivity and the front thickness increased with powder loading, while the temperature gradient and the maximum temperature decreased with solid loading. Due to the relationship between the thermal diffusivity and the microscopic velocity, it has been shown that the RMS velocity is a good candidate for eq 7. The increase in the thermal diffusivity is attributed to the increase in the loading of Al NPs, which consequently increases the thickness of the reaction zone. The decrease in the temperature gradient signifies that the thickness of the reaction zone is affected more than the change in temperature as the loading of Al NPs increases. Uncertainty analysis showed that the temperature gradient is sensitive to the nAl loading, while the maximum temperature is sensitive to the temperature uncertainty. These results provide both a process to analyze thermal waves of thin-film combustion as well as statistical analysis relating flame front microstructure and global properties of a system that can be used to validate computational experiments of combustion systems.

■ ASSOCIATED CONTENT

Supporting Information

The Supporting Information is available free of charge at https://pubs.acs.org/doi/10.1021/acs.jpcc.6c00579.

Includes additional experimental details, and materials and methods, including photographs of the experimental setup (PDF)

■ AUTHOR INFORMATION

Corresponding Author

Michael R. Zachariah − *Department of Chemical and Environmental Engineering, University of California, Riverside, California 92521, United States;* orcid.org/0000-0002-4115-3324; Email: mrz@engr.ucr.edu

Authors

Erik Hagen − *Materials Science and Engineering, University of California, Riverside, California 92521, United States*

Daniel Olsen − *The Woodruff School of Mechanical Engineering, Georgia Institute of Technology, Atlanta, Georgia 30332, United States*

Yuxin Zhou − *Department of Chemical and Environmental Engineering, University of California, Riverside, California 92521, United States;* orcid.org/0009-0005-1397-3834

Min Zhou − *The Woodruff School of Mechanical Engineering, Georgia Institute of Technology, Atlanta, Georgia 30332, United States*

Complete contact information is available at: https://pubs.acs.org/10.1021/acs.jpcc.6c00579

Author Contributions

E.H.: Writing − original draft, Investigation, Data curation. D.O.: Writing − review and editing, Investigation. Y.Z.: SEM and EDS imaging. M.Z.: Writing − review and editing, Methodology. M.Z.: Writing − review and editing, Methodology, Conceptualization.

Notes

The authors declare no competing financial interest.

■ ACKNOWLEDGMENTS

This work was supported by the DTRA-MSEE URA and the ONR.

■ REFERENCES

(1) Wang, H.; Hagen, E.; Shi, K.; Herrera, S.; Xu, F.; Zachariah, M. R. Carbon Fibers as Additives to Engineer Agglomeration and Propagation of Aluminized Propellants. *Chem. Eng. J.* **2023**, *460*, 141653.

(2) Singh, V.; Wu, T.; Hagen, E.; Salvagnac, L.; Tenailleau, C.; Estéve, A.; Zachariah, M. R.; Rossi, C. How Positioning of a Hard Ceramic TiB2 Layer in Al/CuO Multilayers Can Regulate the Overall Energy Release Behavior. *Fuel* **2023**, *349*, 128599.

(3) Joshi, A.; Mer, K. K. S.; Bhattacharya, S.; Patel, V. K. Nano-Aluminium as Catalyst in Thermal Decomposition of Energetic Materials, In *Nano-Energ. Mater.*, Bhattacharya, S.; Agarwal, A. K.; Rajagopalan, T.; Patel, V. K., Eds. Springer: Singapore, 2019; pp. 109−120. .
(4) Riegsinger, S.; Popescu, R.; Gerthsen, D.; Feldmann, C. Room-Temperature Liquid-Phase Synthesis of Aluminium Nanoparticles. *Chem. Commun.* **2022**, *58* (54), 7499−7502.
(5) Thiruvengadathan, R. Aluminum-Based Nano-Energetic Materials: State of the Art and Future Perspectives, In *Nano-Energetic Materials*, Bhattacharya, S.; Agarwal, A. K.; Rajagopalan, T.; Patel, V. K., Eds. Springer: Singapore, 2019; pp. 9−35. .
(6) Yu, Z.; Li, Y.; Guo, T.; Zhang, J.; Wu, S.; Huang, J.; Song, J.; Fang, X. Chemical Reaction Mechanism and Mechanical Response of PTFE/Al/TiH2 Reactive Composites. *J. Mater. Eng. Perform* **2019**, *28* (12), 7493−7501.
(7) Saigal, A.; Joshi, V. S. *Strength and Stiffness of Aluminum/PTFE Reactive Composites*. American Society of Mechanical Engineers Digital Collection, 2021; pp. 107−112. .
(8) Valluri, S. *Development and Analysis of Aluminum-PTFE Reactive Composite Material Theses*; New Jersey Institute of Technology, 2016.
(9) Uhlenhake, K. E.; Yehia, O. R.; Noel, A.; Terry, B. C.; Örnek, M.; Belal, H. M.; Gunduz, I. E.; Son, S. F. On the Use of Fluorine-Containing Nano-Aluminum Composite Particles to Tailor Composite Solid Rocket Propellants. *Propellants, Explos., Pyrotech* **2022**, *47* (7), No. e202100370.
(10) Marshall, J. E.; Zhenova, A.; Roberts, S.; Petchey, T.; Zhu, P.; Dancer, C. E. J.; McElroy, C. R.; Kendrick, E.; Goodship, V. On the Solubility and Stability of Polyvinylidene Fluoride. *Polymers* **2021**, *13* (9), 1354.
(11) Kubota, N.; Serizawa, C. Combustion of Magnesium/Polytetrafluoroethylene. *J. Propuls. Power* **1987**, *3* (4), 303−307.
(12) Wang, Z.; Zhou, W.; Sui, X.; Dong, L. Enhanced Dielectric Properties and Thermal Conductivity of Al/CNTs/PVDF Ternary Composites. *J. Reinf. Plast. Compos* **2015**, *34* (14), 1126−1135.
(13) Zhou, W.; Zuo, J.; Ren, W. Thermal Conductivity and Dielectric Properties of Al/PVDF Composites. *Compos. Part Appl. Sci. Manuf.* **2012**, *43* (4), 658−664.
(14) Rehwoldt, M. C.; Wang, H.; Kline, D. J.; Wu, T.; Eckman, N.; Wang, P.; Agrawal, N. R.; Zachariah, M. R. Ignition and Combustion Analysis of Direct Write Fabricated Aluminum/Metal Oxide/PVDF Films. *Combust. Flame* **2020**, *211*, 260−269.
(15) Rehwoldt, M. C.; Wang, Y.; Xu, F.; Ghildiyal, P.; Zachariah, M. R. High-Temperature Interactions of Metal Oxides and a PVDF Binder. *ACS Appl. Mater. Interfaces* **2022**, *14* (7), 8938−8946.
(16) Wang, H.; Rehwoldt, M.; Kline, D. J.; Wu, T.; Wang, P.; Zachariah, M. R. Comparison Study of the Ignition and Combustion Characteristics of Directly-Written Al/PVDF, Al/Viton and Al/THV Composites. *Combust. Flame* **2019**, *201*, 181−186.
(17) De Lisio, J. B.; Hu, X.; Wu, T.; Egan, G. C.; Young, G.; Zachariah, M. R. Probing the Reaction Mechanism of Aluminum/Poly(Vinylidene Fluoride) Composites. *J. Phys. Chem. B* **2016**, *120* (24), 5534−5542.
(18) Daniel, O.; Hagen, E.; Zachariah, M.; Zhou, M. *Combustion Reaction Dynamics of Nano-Aluminum and PVDF Composites Part II: multiscale Computational Simulations*, DOI: 10.1021/acs.jpcc.6c00580.
(19) Wang, Y.; Hagen, E.; Biswas, P.; Wang, H.; Zachariah, M. R. Imaging the Combustion Characteristics of Al, B, and Ti Composites. *Combust. Flame* **2023**, *252*, 112747.
(20) Wang, H.; Julien, B.; Kline, D. J.; Alibay, Z.; Rehwoldt, M. C.; Rossi, C.; Zachariah, M. R. Probing the Reaction Zone of Nanolaminates at ∼ μs Time and ∼ μm Spatial Resolution. *J. Phys. Chem. C* **2020**, *124* (25), 13679−13687.
(21) Jacob, R. J.; Kline, D. J.; Zachariah, M. R. High Speed 2-Dimensional Temperature Measurements of Nanothermite Composites: Probing Thermal vs. Gas Generation Effects. *J. Appl. Phys.* **2018**, *123* (11), 115902.
(22) Kline, D. J.; Rehwoldt, M. C.; De Lisio, J. B.; Barron, S. C.; Wang, H.; Alibay, Z.; Rodriguez, J. C.; Fritz, G. M.; Zachariah, M. R. In-Operando Thermophysical Properties and Kinetics Measurements of Al-Zr-C Composites. *Combust. Flame* **2021**, *228*, 250−258.
(23) Kline, D. J.; Alibay, Z.; Rehwoldt, M. C.; Idrogo-Lam, A.; Hamilton, S. G.; Biswas, P.; Xu, F.; Zachariah, M. R. Experimental Observation of the Heat Transfer Mechanisms That Drive Propagation in Additively Manufactured Energetic Materials. *Combust. Flame* **2020**, *215*, 417−424.
(24) Granier, J. J.; Pantoya, M. L. The Effect of Size Distribution on Burn Rate in Nanocomposite Thermites: A Probability Density Function Study. *Combust. Theory Model* **2004**, *8* (3), 555−565.
(25) De Luca, L. T.; Galfetti, L.; Colombo, G.; Maggi, F.; Bandera, A.; Babuk, V. A.; Sinditskii, V. P. Microstructure Effects in Aluminized Solid Rocket Propellants. *J. Propuls. Power* **2012**.
(26) Örnek, M.; Uhlenhake, K. E.; Zhou, Y.; Zhang, B.; Kalaswad, M.; Collard, D. N.; Wang, H.; Wang, Q.; Son, S. F. Preparation and Characterization of Multifunctional Piezoenergetic Polyvinylidene Fluoride/Aluminum Nanocomposite Films. *J. Appl. Phys.* **2022**, *131* (5), 055108.
(27) Kline, D. J.; Rehwoldt, M. C.; Wang, H.; Eckman, N. E.; Zachariah, M. R. Why Does Adding a Poor Thermal Conductor Increase Propagation Rate in Solid Propellants? *Appl. Phys. Lett.* **2019**, *115* (11), 114101.
(28) Wang, H.; Jiang, Y.; Wang, Y.; Kline, D. J.; Zheng, X.; Zachariah, M. R. Do We Need Perfect Mixing between Fuel and Oxidizer to Maximize the Energy Release Rate of Energetic Nanocomposites? *Appl. Phys. Lett.* **2023**, *122* (1), 011901.
(29) Pelzmann, T.; Dupont, F.; Sauté, B.; Robert, É. Surface Temperature and Emissivity Measurement for Materials Exposed to a Flame through Two-Color IR-Thermography. *arXiv* **2022**.
(30) Kalman, J.; Hedman, T. On the Origin and Use of the Emissivity Approximations for Alumina Particles. *Propellants, Explos., Pyrotech* **2016**, *41* (5), 793−797.
(31) Jones, J. M.; Mason, P. E.; Williams, A. A Compilation of Data on the Radiant Emissivity of Some Materials at High Temperatures. *J. Energy Inst.* **2019**, *92* (3), 523−534.
(32) Natarajan, J.; Lieuwen, T.; Seitzman, J. Laminar Flame Speeds of H2/CO Mixtures: Effect of CO2 Dilution, Preheat Temperature, and Pressure. *Combust. Flame* **2007**, *151* (1), 104−119.
(33) Askari, O.; Wang, Z.; Vien, K.; Sirio, M.; Metghalchi, H. On the Flame Stability and Laminar Burning Speeds of Syngas/O2/He Premixed Flame. *Fuel* **2017**, *190*, 90−103.
(34) Blint, R. J. The Relationship of the Laminar Flame Width to Flame Speed. *Combust. Sci. Technol.* **1986**, *49* (1−2), 79−92.
(35) Leitner, M.; Leitner, T.; Schmon, A.; Aziz, K.; Pottlacher, G. Thermophysical Properties of Liquid Aluminum. *Metall. Mater. Trans. A* **2017**, *48* (6), 3036−3045.
(36) Roy, S. Calculation of Heat of Polymerisation: Group-Contribution Method. *Polym. Bull* **1999**, *42* (2), 229−236.
(37) Li, J.; Liu, X.; Xie, Q.; Su, J.; Hu, M.; Yao, Z. Effect of Perchlorate on Combustion Properties of Directly-Written Al/PVDF Composites. *Fire* **2023**, *6* (3), 106.
(38) Ameduri, B. From Vinylidene Fluoride (VDF) to the Applications of VDF-Containing Polymers and Copolymers: Recent Developments and Future Trends. *Chem. Rev.* **2009**, *109* (12), 6632−6686.
(39) Chase, M. W.; Sauerwein, J. C. *NIST Standard Reference Data Products 1991 Catalog*. National Institute of Standards and Technology, 1990.
(40) Ackermann, T. Thermochemical kinetics. Methods for the estimation of thermochemical data and rate parameters. Von S. W. Benson. John Wiley & Sons, Inc., New York 1976. 2. Aufl., XI, 320 S., 15 Abb., geb. $ 28.50. *Angew. Chem.* **1977**, *89* (12), 921.